Current Harmonic Suppression in Dual Three-Phase Permanent Magnet Synchronous Machine With Extended State Observer

Yongxiang Xu, *Member, IEEE*, Boyuan Zheng, Guan Wang, Hao Yan, *Member, IEEE*, and Jibin Zou, *Senior Member, IEEE*

***Abstract*—Dual three-phase (DTP) permanent magnet synchronous machines (PMSM) have been utilized in many applications due to their outstanding performance. However, large stator current harmonics limit the further application of the DTP-PMSM due to the low impedance in the harmonic subspace. To solve this problem, this article proposes a current harmonic suppression strategy based on an extended state observer (ESO). A detailed analysis is carried out to demonstrate the disturbance rejection ability and robustness of the proposed method. The theoretical analysis also shows that the ESO strategy outstands the conventional proportional-integral controller and advanced proportional resonance (PR) controller in terms of harmonic reduction. The advantages are verified by simulation and experimental results under different operating conditions. The proposed strategy still works well when considering other factors that may cause harmonic distortion, such as magnetic circuit saturation, saliency ratio, over-modulation of the inverter, the voltage drop caused by electric devices, and dead time. Meanwhile, some limitations are also pointed out. The proposed strategy can also be easily applied to other multiphase PMSM types.**

***Index Terms*—Dual three-phase (DTP), current control, extended state observe (ESO), harmonics, permanent magnet synchronous machines (PMSM), stability.**

NOMENCLATURE

u_s	Phase voltage in stationary frame.
R_s	Stator resistance.
ψ_s	Magnetic flux in stationary frame.
p_n	Number of pole pairs.
θ	Electrical angle.
J	Rotational inertia.
T_L	Load torque.
x_1,x_2	State variables.
z_3	Estimate value of the disturbance.
b_0	Proportion constant of the input in ESO.
i_z	Current in z1-z2 subspace.
d	Disturbance.
k_p, k_i	Parameters of the ESO.
ω_0	Bandwidth of ESO.
^	Estimated value.
$U_{\rm dc}$	DC voltage.
i_s	Phase current in stationary frame.
L_s	Stator inductance (stationary frame).
ψ_{fd}	Magnetic flux of the permanent magnet.
T_e	Electromagnetic torque.
ω_m	Mechanical angular speed.
B	Damping factor.
L_{aa1}	Leakage inductance.
z_1,z_2	Estimate value of the state variables.
β_{01}, β_{02}	Parameters of ESO.
u	Input of ESO.
u_z	Voltage in $z1$-$z2$ subspace.
f	Total disturbance.
T_s	Sampling period.
ω_c, ω_e	Bandwidth of PR controller.
$\rm V_1$	Phase voltage amplitude.
L_0, L_2	Fundamental and second harmonic amplitude of the self-inductance.

Manuscript received November 9, 2019; revised March 18, 2020; accepted April 14, 2020. Date of publication April 21, 2020; date of current version July 20, 2020. This work was supported by the National Natural Science Foundation of China under Grants 51437004, 51577036, and 51521003. Recommended for publication by Associate Editor W. Cao. *(Corresponding author: Boyuan Zheng.)*

Yongxiang Xu, Boyuan Zheng, Guan Wang, and Jibin Zou are with the School of Electrical Engineering, Harbin Institute of Technology, Harbin 150001, China (e-mail: xuyx@hit.edu.cn; zhengboyuan_hit@outlook.com; wghit@outlook.com; zoujibin@hit.edu.cn).

Hao Yan is with the School of Electrical and Electronic Engineering, Nanyang Technological University, Singapore 639798, Singapore (e-mail: yanhaohit@yahoo.com).

Color versions of one or more of the figures in this article are available online at https://ieeexplore.ieee.org.

Digital Object Identifier 10.1109/TPEL.2020.2989624

I. INTRODUCTION

THE permanent magnet synchronous machines (PMSM) has been widely used for its merits of high power density, high efficiency, and high torque–current ratio. Nevertheless, it might cost much to utilize the conventional three-phase PMSM in the high-power situations owing to the expensive high-volume power electronic devices. An effective strategy to solve this issue is the multiphase strategy [1]–[4]. Multiphase PMSMs have the advantage of reducing the burden of inverters and improving the fault-tolerant ability [5]–[8]. They are especially suitable for applications such as electric vehicles, railways, and aircraft propulsion [9], [10]. A favorable choice of multiphase machines is the dual three-phase (DTP)-PMSM. It has two sets of three-phase stator windings spatially shifted by 30 electrical degrees with isolated neutral points. The lowest order of the torque ripple in DTP-PMSM is 12th, hence promoting the performance of the output torque, compared with conventional three-phase PMSM

with the 6th torque ripple. Nevertheless, large stator harmonic current occurs in DTP-PMSM due to the small harmonic impendence covering stator resistance and leakage inductance. The harmonic current will lead to the efficiency decrease and control performance degradation of the system. As a result, it is quite important to suppress the harmonic current in DTP-PMSM.

Although the stator current harmonic problem in multiphase machines is widely recognized and has been known for a long time, the research on harmonic suppression in multiphase machines is not quite popular until the last decade. The current harmonic might be affected by a lot of factors such as the structure of the machines, nonlinearity of the inverter, existence of dead time, modulation strategies, modulation index, operating speed, and magnetic circuit saturation. The predictive current controller is used to suppress the harmonic current in [11]. However, predictive control relies on the precise model of the system, which will induce an extra calculation burden. The resonant controller is introduced in [12], but certain frequencies in the current components might lead to resonance in the system. Twelve new synthetic voltage vectors are proposed in [13], in which the variables related to torque production are well controlled in direct torque control strategies. However, the effectiveness of this strategy is not verified in field-oriented control, and the new vector combination is complicated to realize. An improved pulsewidth modulation (PWM) strategy was proposed to deal with the harmonic distortion in the overmodulation region [9], but it only considers partial current harmonics. In [14], a disturbance observer was utilized. The model predictive control strategy is improved in [15], achieving a better harmonic suppression ability but still relying heavily on the precise model of the system. Moreover, the enhanced harmonic models are built in [16]. The enhanced harmonic models introduce an improved vector control scheme for the DTP-PMSM system but only part of the harmonic problem is solved. The strategies aforementioned have incorporated some active control strategies. However, the accuracy of most of the strategies is heavily dependent on a precise objective model, which increases the burden of the calculation. In practical, it is not possible to get the precise model, so the existing strategies just solve the current harmonic issue to a certain extent. Thus, more actions should be taken for further improvement.

The extended state observer (ESO) proposed in [17] has advantages over conventional observers in the following aspects. The design of ESO is independent of an accurate mathematical model. It is also robust and has good dynamic performance [18]–[21]. As a consequence, the ESO has been regarded as an effective feed-forward strategy to cooperate with other control strategies [22]. In the DTP-PMSM, the uncertainty of the harmonic current can be regarded as a kind of unknown disturbance and can be estimated by ESO with high accuracy and fast dynamic response. Compared to the existing harmonic current suppression strategies, it has many advantages. Unlike model predictive control, its performance does not rely on the accuracy of the model. It would not induce resonance or instability to the system and it is also suitable for variable speed situations without extra modification, which outweighs the resonant controller. Unlike many strategies only focus on certain orders of the harmonic current [14] or certain parts of the harmonic current [9], [16], the strategy based on ESO can cover all orders of harmonic current components and can eliminate them thoroughly in theory.

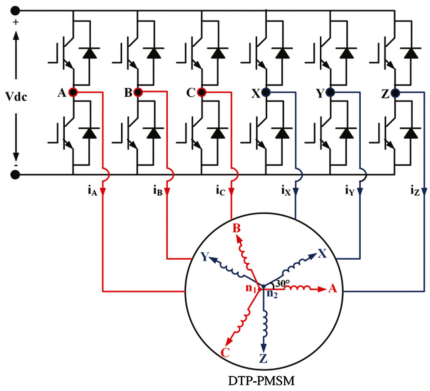

Fig. 1. DTP-PMSM system.

The rest of this article is organized as follows. The mathematical model of DTP-PMSM is introduced in Section II. The proposed harmonic suppression strategy is designed and analyzed in Section III, proving the theoretical privilege of this strategy. Section IV studies the applicability and limitations of the proposed strategy. Section V verifies the effectiveness of the proposed control strategy by comparison with the conventional proportional–integral (PI) controller and proportional resonance (PR) controller through simulations and experiments on a DTP-PMSM drive system. The key contributions are also highlighted and validated. Finally, Section VI concludes this article.

II. Operation Principle of DTP-PMSM

A simple but precise DTP-PMSM model is the foundation of its optimization and control. Compared with the conventional three-phase PMSM, the DTP-PMSM has a more complicated electromagnetic characteristic. The following assumptions are proposed to simplify the analysis in building the model.

a) The parameters and the structure in each phase are the same.
b) The magnetic circuit is linear and its saturation is ignored.
c) The skin effect and temperature effect are neglected.
d) The slot effect, damp winding, and eddy effect are neglected.

The DTP-PMSM system fed by voltage source inverter (VSI) is shown in Fig. 1. In the stationary frame, the voltage equation can be expressed as (1). The flux equation can be given as (2). Based on the method of virtual displacement, the torque equation can be calculated as (3). And the equation of mechanical motion is given as (4)

$$
\begin{aligned}
u_s &= R_s i_s + \frac{d\psi_s}{dt} \\
u_s &= \begin{bmatrix} u_A & u_B & u_C & u_X & u_Y & u_Z \end{bmatrix}^T \\
\gamma_s &= \begin{bmatrix} \cos\theta & \cos(\theta - \frac{2\pi}{3}) & \cos(\theta + \frac{2\pi}{3}); \\ \cos(\theta - \frac{\pi}{6}) & \cos(\theta - \frac{5\pi}{6}) & \cos(\theta + \frac{\pi}{2}) \end{bmatrix}^T
\end{aligned} \tag{1}
$$

$$\psi_s = L_s i_s + \gamma_s \psi_{fd} \tag{2}$$

$$T_e = p_n \left(\frac{1}{2} i_s^T \frac{\partial L_s}{\partial \theta} i_s + i_s^T \frac{\partial \gamma}{\partial \theta} \psi_{fd} \right) \tag{3}$$

$$\frac{d\omega_m}{dt} = \frac{1}{J}(T_e - B\omega_m - T_L). \tag{4}$$

The machine parameters and variables in (1)–(4) are defined in the nomenclature.

In the stationary frame, the coupled matrix of inductance makes it hard to analyze and control. In dual three-phase machines, the conventional decoupling method is not effective anymore so that the vector space decomposition (VSD) method should be applied. According to the VSD theory, the variables of the DTP-PMSM can be mapped into three mutually orthogonal subspaces, α-β subspace, z_1-z_2 subspace and o_1-o_2 subspace, respectively [24]. Different orders of harmonics are mapped into different subspaces. The fundamental wave and the harmonics with the order $12n\pm1 (n = 1,2,3,\ldots)$ are mapped into the α-β subspace, the harmonics with the order $6n\pm1 (n = 1,3,5,\ldots)$ are mapped into the z_1-z_2 subspace, the harmonics with the order $6n\pm3 (n = 1,3,5,\ldots)$ are mapped into the o_1-o_2 subspace, respectively. The decoupling transformation matrix is shown in (5), at the bottom of this page [24].

Since only the components in the α-β subspace are relative to the energy conversion, it is only necessary to transform the α-β components into the synchronous reference frame. So the transformation matrix from the original stationary coordinate system (ABC, DEF) to the rotating coordinate system (d-q, $z1$-$z2$) is shown in (6), shown at the bottom of this page.

The corresponding equations of voltage, flux, and torque are shown as

$$\begin{bmatrix} u_d \\ u_q \\ u_{z1} \\ u_{z2} \end{bmatrix} = \begin{bmatrix} R & 0 & 0 & 0 \\ 0 & R & 0 & 0 \\ 0 & 0 & R & 0 \\ 0 & 0 & 0 & R \end{bmatrix} \begin{bmatrix} i_d \\ i_q \\ i_{z1} \\ i_{z2} \end{bmatrix} + \begin{bmatrix} \dot{\psi}_d \\ \dot{\psi}_q \\ \dot{\psi}_{z1} \\ \dot{\psi}_{z2} \end{bmatrix} + \omega \begin{bmatrix} -\psi_q \\ \psi_d \\ 0 \\ 0 \end{bmatrix} \tag{7}$$

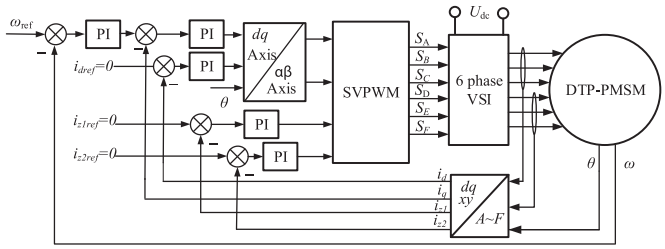

Fig. 2. Four-dimensional vector control topological graph.

$$\begin{bmatrix} \psi_d \\ \psi_q \\ \psi_{z1} \\ \psi_{z2} \end{bmatrix} = \begin{bmatrix} L_D & 0 & 0 & 0 \\ 0 & L_Q & 0 & 0 \\ 0 & 0 & L_{aa1} & 0 \\ 0 & 0 & 0 & L_{aa1} \end{bmatrix} \begin{bmatrix} i_d \\ i_q \\ i_{z1} \\ i_{z2} \end{bmatrix} + \begin{bmatrix} 1 \\ 0 \\ 0 \\ 0 \end{bmatrix} \psi_{fd} \tag{8}$$

$$T_e = 3p_n \left[(L_D - L_Q)\, i_d i_q + i_q \psi_{fd} \right]. \tag{9}$$

The control scheme of the DTP-PMSM includes the two-dimensional vector control and the four-dimensional vector control [25]–[27]. The two-dimensional vector control only controls the current in α-β subspace, which is related to the energy conversion. As for the current in z_1-z_2 subspace, the open-loop control scheme is utilized. The reference voltage in z_1-z_2 subspace is given zero to suppress the harmonic current. However, the 5th and 7th harmonic voltages still exist, therefore causing severe current harmonics. The four-dimensional vector control suppresses the harmonic current in z_1-z_2 subspace with closed-loop control. Nevertheless, it is more difficult to implement. The topology of the four-dimensional vector control is shown in Fig. 2.

The PWM strategy is one of the most important research topics in multiphase motors. With the increase of the phases, the switching states go through exponential growth, which brings abundant control resources as well as the difficulty in modulation algorithm. The common PWM strategies in DTP-PMSM include the two-vector SVPWM, the four-vector SVPWM [28], [29], and the three-phase decomposition SVPWM [30], [31]. Their abilities in overmodulation, harmonic suppression, and the degree of

$$T_{62s} = \frac{1}{3} \begin{bmatrix} 1 & -\frac{1}{2} & -\frac{1}{2} & \frac{\sqrt{3}}{2} & -\frac{\sqrt{3}}{2} & 0 \\ 0 & \frac{\sqrt{3}}{2} & -\frac{\sqrt{3}}{2} & \frac{1}{2} & \frac{1}{2} & -1 \\ 1 & -\frac{1}{2} & -\frac{1}{2} & -\frac{\sqrt{3}}{2} & \frac{\sqrt{3}}{2} & 0 \\ 0 & -\frac{\sqrt{3}}{2} & \frac{\sqrt{3}}{2} & \frac{1}{2} & \frac{1}{2} & -1 \\ 1 & 1 & 1 & 0 & 0 & 0 \\ 0 & 0 & 0 & 1 & 1 & 1 \end{bmatrix} \tag{5}$$

$$T_{62} = \begin{bmatrix} \cos\theta & \cos(\theta - \frac{2\pi}{3}) & \cos(\theta + \frac{2\pi}{3}) & \cos(\theta - \frac{\pi}{6}) & \cos(\theta - \frac{5\pi}{6}) & \cos(\theta + \frac{\pi}{2}) \\ -\sin\theta & -\sin(\theta - \frac{2\pi}{3}) & -\sin(\theta + \frac{2\pi}{3}) & -\sin(\theta - \frac{\pi}{6}) & -\sin(\theta - \frac{5\pi}{6}) & -\sin(\theta + \frac{\pi}{2}) \\ 1 & -\frac{1}{2} & -\frac{1}{2} & -\frac{\sqrt{3}}{2} & \frac{\sqrt{3}}{2} & 0 \\ 0 & -\frac{\sqrt{3}}{2} & \frac{\sqrt{3}}{2} & \frac{1}{2} & \frac{1}{2} & -1 \\ 1 & 1 & 1 & 0 & 0 & 0 \\ 0 & 0 & 0 & 1 & 1 & 1 \end{bmatrix}. \tag{6}$$

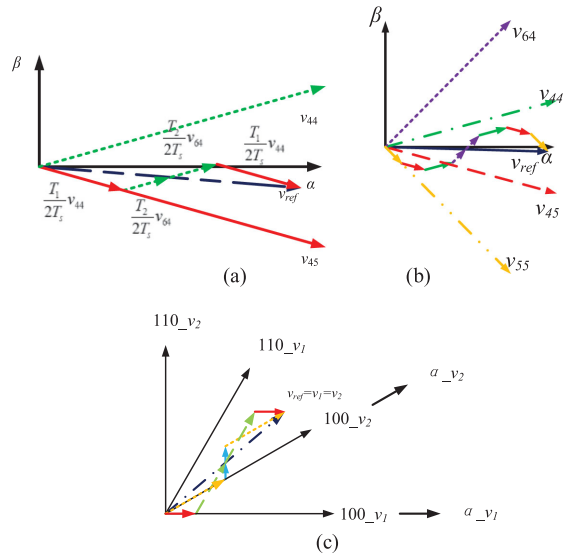

Fig. 3. Composition of vector v_{ref} in different SVPWM strategies. (a) Two vector SVPWM. T_1 is the duration of voltage vector v_{44}, T_2 is the duration of voltage vector v_{45}. T_0 is the duration of zero vector, which is chosen as v_{00} and v_{77} here. (b) Four vector SVPWM in α-β subspace. (c) Three-phase decomposition SVPWM when $v_{z1-z2}=0$, v_1, v_2 is the reference vector in α_$v1$, α_$v2$ subspace.

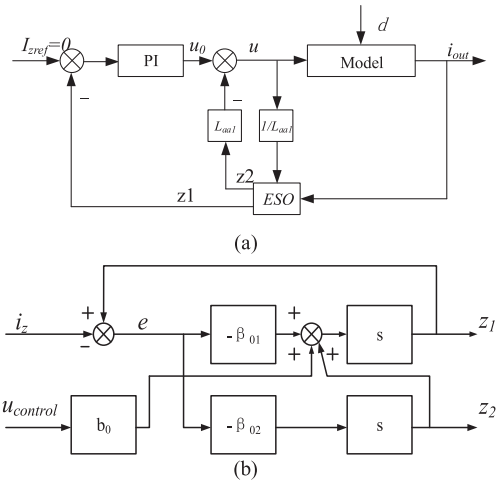

Fig. 4. Control loop in the z_1-z_2 subspace. (a) Control loop in z1-z2 subspace. (b) Inner structure of the ESO.

difficulty in implementation are different. The maximum limit of the modulation index ($|V_1|/U_{DC}$) of two-vector SVPWM is 0.622. For four-vector SVPWM and three-phase decomposition SVPWM, it is 0.577. Taking Section 12 as an example, the composition of the reference vector v_{ref} in these three SVPWM strategies can be shown in Fig. 3.

According to (6)–(8), the voltage in z_1-z_2 subspace is not transformed to *d*-*q* axis, so u_{z1} and u_{z2} are not dc components but sine-wave signals. So, the PI controller in Fig. 2 cannot eliminate the harmonics currents well in theory. Therefore, a new harmonic suppression strategy is proposed in this article to cope with this issue.

III. Proposed Harmonic Suppression Strategy

As mentioned before, obvious harmonic current can be observed when operating the DTP-PMSM with the conventional control scheme. Although the 5th and 7th stator harmonic current would not produce the torque ripple, it will reduce the efficiency of the system and deteriorate the control performance.

A. Design of ESO

There are two main sources of the harmonic current in the DTP-PMSM system. The first source is the inverters and the second one is the internal structure of the PMSM itself, which means that the current harmonics are induced by both the internal and external disturbances. They can be modeled as a lumped disturbance acting on the input of the model.

ESO is first introduced as part of active disturbance rejection control. The proposed plant is augmented with a fictitious disturbance model and the state observer is constructed to estimate the states of the plants and the state of the disturbance model [14]. The basic idea of ESO can be described as lumping all the inner and outer nonlinearities, uncertainties, and disturbances as a total disturbance. Compared with other state observers, ESO can observe not only the state variables but also the extended variable. The estimated total disturbance can be exploited for compensation by the control law in real time.

Taking the 1st order system as an example, the basic theory of the linear ESO can be described as

$$\begin{cases} e = z_1 - x_1 \\ \dot{z}_1 = z_2 - \beta_{01} e + b_0 u \\ \dot{z}_2 = -\beta_{02} e. \end{cases} \tag{10}$$

where only β_{01} and β_{02} are parameters to be tuned. Since the aim of this control strategy is to eliminate the current harmonic and the main source of the harmonic is the 5th and 7th harmonic current that are located on the z_1-z_2 subspace, the ESO is utilized only on the z_1-z_2 subspace in this article. The equation in z1-z2 subspace shown in (7) can be expressed by (11) considering the disturbance

$$\dot{i}_z = -\frac{R}{L_{aa1}} i_z + \frac{1}{L_{aa1}} u_z + d = f + \frac{1}{L_{aa1}} u_z. \tag{11}$$

And, the model can be derived as

$$\begin{cases} \dot{x}_1 = x_2 + \frac{1}{L_{aa1}} u_z \\ \dot{x}_2 = f' \\ y = x_1 \end{cases} \tag{12}$$

where $y = x_1 = i_z$. The format of the system in (12) is the standard system format of ESO. So a first-order ESO can be utilized in this subspace, which can be expressed by (13). The structure of the control loop in z_1-z_2 subspace can be shown in Fig. 4(a), and the inner structure of the ESO can be shown in Fig. 4(b). Compared to the conventional current loop in z_1-z_2 subspace, the PI controller remains the same, just adding the ESO in the feedback path. The input of the ESO is the actual current in z_1-z_2 subspace and the input voltage of the PMSM. The outputs of the ESO are the estimate of the subspace current

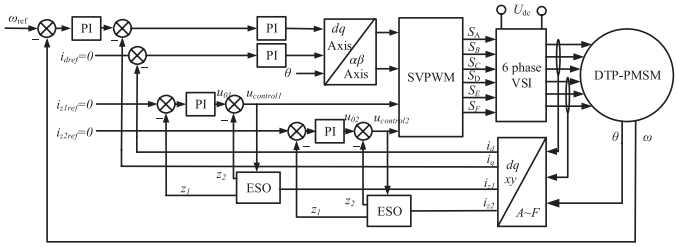

Fig. 5. Block diagram of the proposed current suppression strategy based on ESO.

z_1 and the estimate of the disturbance z_2. The new control scheme with the ESO replaces the current feedback with its estimate z_1 and uses z_2 as a feedforward part to eliminate the disturbance in the system so as to suppress the current harmonic in z_1-z_2 subspace

$$\begin{cases} e = z_1 - x_1 \\ \dot{z}_1 = z_2 - \beta_{01} e + \frac{1}{L_{aa1}} u_z \\ \dot{z}_2 = -\beta_{02} e. \end{cases} \tag{13}$$

The closed-loop control law can be expressed by as

$$\begin{cases} e_{1r} = y^* - z_1 \\ u = \frac{k_I + k_P s}{s} e_{1r} - L_{aa1} z_2 \end{cases} \tag{14}$$

where $y* = I_{\text{zref}}$ is the input reference of the closed control loop, and k_p and k_i are the proportional and integral gains of the PI controller, respectively. The overall control scheme including the ESO is presented in Fig. 5.

B. Performance Analysis of the Extend State Observer

Based on (13), the estimated state variable and total disturbance can be obtained as

$$\begin{cases} \hat{i}_z = z_1 = \frac{(\beta_{02} + \beta_{01} s) x_1 + \frac{s}{L_{aa1}} u_z}{s^2 + \beta_{01} s + \beta_{02}} \\ \hat{f} = z_2 = \frac{\beta_{02} s^2 x_1 - \frac{s \beta_{02}}{L_{aa1}} u_z}{s^2 + \beta_{01} s + \beta_{02}} \end{cases} \tag{15}$$

where$\hat{i}_z$, $\hat{f}$ is the estimate of i_z, f. and according to (12) and (13)

$$\begin{cases} e_1 = z_1 - x_1, e_2 = z_2 - x_2 \\ \frac{de_1}{dt} = \frac{dz_1}{dt} - \frac{dx_1}{dt} = e_2 - \beta_{01} e_1 \\ \frac{de_2}{dt} = \frac{dz_2}{dt} - \frac{dx_2}{dt} = -\beta_{02} e_1 - f'(t). \end{cases} \tag{16}$$

Transform (16) into s-domain and the solution can be derived as

$$\begin{cases} e_1 = -\frac{s}{s^2 + \beta_{01} s + \beta_{02}} x_2 = -\frac{s}{s^2 + \beta_{01} s + \beta_{02}} (s x_1 - \frac{1}{L_{aa1}} u_{z1}) \\ e_2 = -\frac{s(s + \beta_{01})}{s^2 + \beta_{01} s + \beta_{02}} x_2. \end{cases} \tag{17}$$

According to (15), (17), and superposition theory, the following transfer function can be derived:

$$\frac{z_1}{x_1} = \frac{\beta_{01} s + \beta_{02}}{s^2 + \beta_{01} s + \beta_{02}}$$
$$\frac{z_2}{x_2} = \frac{\beta_{02}}{s^2 + \beta_{01} s + \beta_{02}}$$

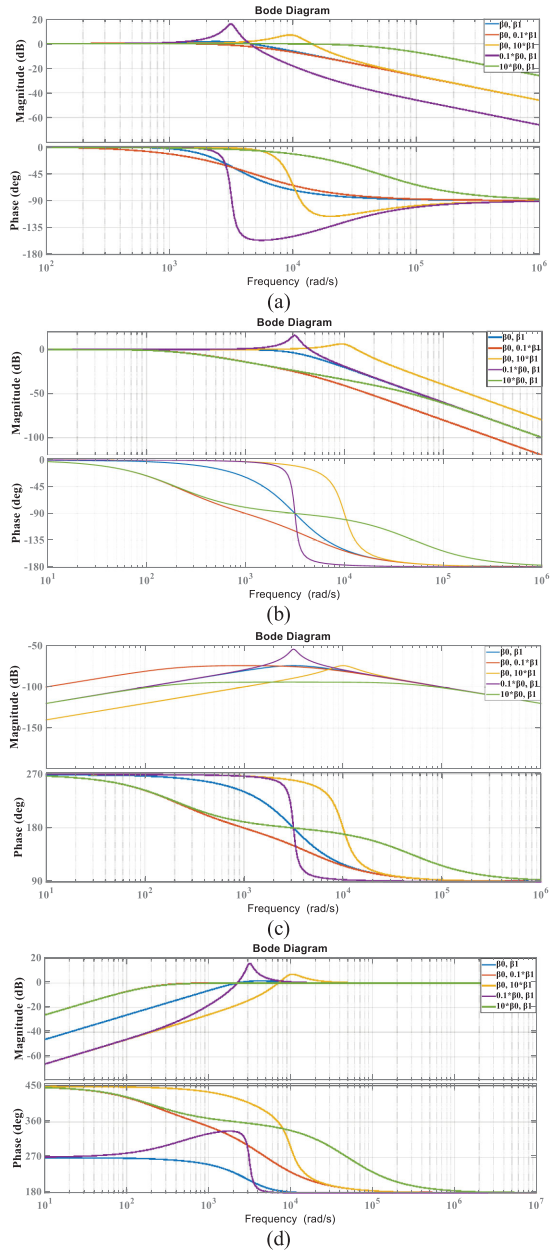

Fig. 6. Bode diagram of ESO. (a) z_1/x_1. (b) z_2/x_2. (c) e_1/x_2. (d) e_2/x_2.

$$\frac{e_1}{x_2} = -\frac{s}{s^2 + \beta_{01} s + \beta_{02}}$$
$$\frac{e_2}{x_2} = -\frac{s(s + \beta_{01})}{s^2 + \beta_{01} s + \beta_{02}}$$
$$\frac{z_1}{u_z} = \frac{s}{s^2 + \beta_{01} s + \beta_{02}} \frac{1}{L_{aa1}}$$
$$\frac{z_2}{u_z} = -\frac{\beta_{02} s}{s^2 + \beta_{01} s + \beta_{02}} \frac{1}{L_{aa1}}. \tag{18}$$

The bode diagrams of each transfer function in (8) are presented in Fig. 6. Several sets of β_{01} and β_{02} parameters are compared with the basic values $\beta_{01}= 5 \times 10^3, \beta_{02}= 6.25 \times 10^6$ [23]. Considering that the transfer functions of z_1/u_z, z_2/u_z

has the same amplitude–frequency characteristics with that of e_1/x_2, whose diagrams are not presented here.

The diagram indicates the following.

1) The bandwidth of z_1/x_1 increases with the increase of β_{01} and β_{02}. And, β_{01} has a more obvious influence.
2) The bandwidth of z_1/x_2 is mainly decided by β_{01}/β_{02}, and the bandwidth increases with the decrease of ratio.
3) The diagrams of e_1/x_2 and e_2/x_2 both have a very low gain at the passband of ESO, which shows the ability in disturbance suppression of the ESO.
4) The error of the disturbance (z_2) is larger than that of the state variable (z_1). And, the disturbance tracking ability is mainly decided by β_{01}/β_{02} and decreases with the decrease of β_{01}/β_{02}.

By properly tuning the parameters β_{01} and β_{02}, the ESO can meet the requirement of the system. In order to tune fewer parameters, according to [23], all the poles of the observer should be placed at $-\omega_0$, where ω_0 represents the bandwidth of the observer, i.e.,$\beta_{01}= 2\omega_0, \beta_{02} = \omega_0^2$. Since the observer would be implement in discrete domain, the Tustin's bilinear rule $s = 2(1 - z^{-1})/[T_s(1 + z^{-1})]$ is utilized. So the characteristic polynomial of the observer in the discrete domain is

$$[(\omega_0 T_s - 2) + (2 + \omega_0 T_s)z]^2. \tag{19}$$

There are two same poles for the discrete observer $p_z = (2 - \omega_0 T_s)/(2 + \omega_0 T_s)$. In order to keep the tracking results from oscillation, p_z should be in the range of (0,1), i.e.,$0 < \omega_0 < 2/T_s$. Fig. 7 is carried out to investigate the effect of ω_0 in ESO.

Compared with Fig. 6, utilizing the relationship between β_{01} and β_{02} will lead to a better disturbance suppression ability. From Fig. 6(a) and (b), we can conclude that as ω_0 becomes larger, the bandwidth of z_1/x_1, z_2/x_2, which represents the range that ESO is effective, will increase. Fig.6(c) and (d) show that as ω_0 increases, both the suppression ability and the suppression range rise. A larger ω_0 will induce the component of a higher frequency into the passband, which will further cause the noise problem. On the other hand, the proposed ESO should trace at least 13th harmonic current of $\omega_0 \in (2250, 20000)$ should be chosen.

C. Performance Analysis of the Closed Loop Controller

To evaluate the performance of the proposed closed-loop controller, (12) and (13) are substituted into (14), which gives the following:

$$\frac{s^2 + \frac{k_P}{L_{aa1}}s + \frac{k_I}{L_{aa1}}}{s}x_1 = \frac{\frac{k_P}{L_{aa1}}s + \frac{k_I}{L_{aa1}}}{s}y^* + \frac{s^2 + (\frac{k_P}{L_{aa1}} + \beta_{01})s + \frac{k_I}{L_{aa1}}}{s^2 + \beta_{01}s + \beta_{02}}x_2. \tag{20}$$

The closed-loop transfer function from the reference input $(y*)$ to the system output $(y = x_1)$ and the sensitive transfer function from the total disturbance $(x_2 = f)$ to the system output $(y = x_1)$ are derived as follows:

$$G_1 = \frac{y}{y^*} = \frac{\frac{k_P}{L_{aa1}}s + \frac{k_I}{L_{aa1}}}{s^2 + \frac{k_P}{L_{aa1}}s + \frac{k_I}{L_{aa1}}} \tag{21}$$

$$G_2 = \frac{y}{f} = \frac{s^3 + (\frac{k_P}{L_{aa1}} + \beta_{01})s^2 + \frac{k_I}{L_{aa1}}s}{(s^2 + \beta_{01}s + \beta_{02})(s^2 + \frac{k_P}{L_{aa1}}s + \frac{k_I}{L_{aa1}})}. \tag{22}$$

G_1 reflects the tracking performance of the closed-loop controller and G_2 reflects the antidisturbance ability of the strategy. The bode diagrams of the transfer functions with different bandwidth ω_0 are shown in Fig. 8.

The bode diagram shows that the tracking performance of the proposed closed-loop control scheme is not affected by

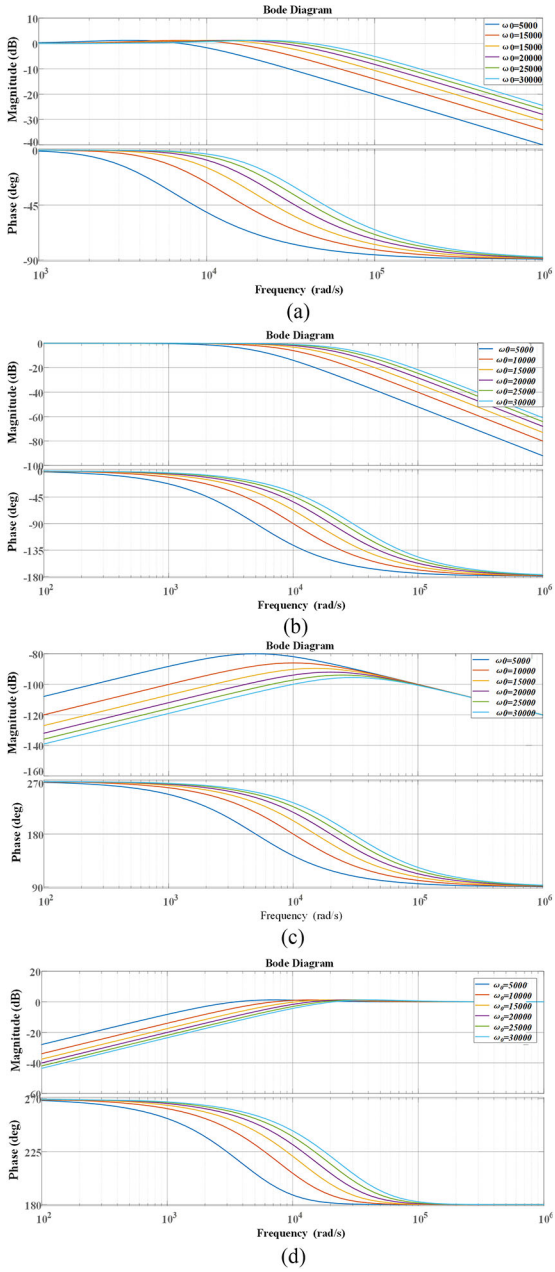

Fig. 7. Bode diagram of ESO with different ω_0. (a) z_1/x_1. (b) z_2/x_2. (c) e_1/x_2. (d) e_2/x_2.

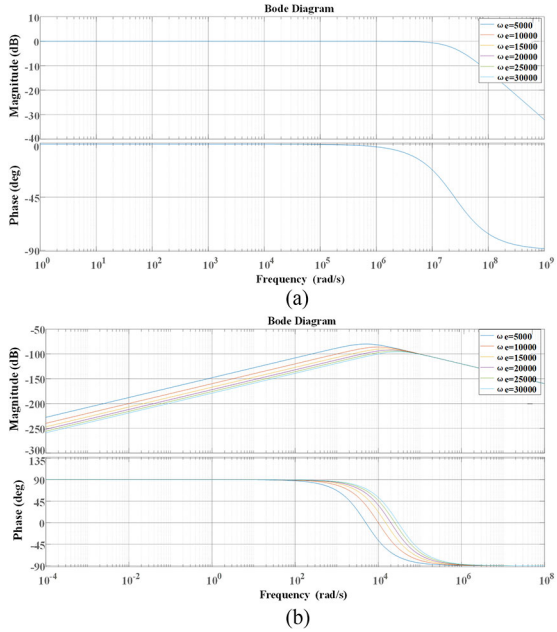

Fig. 8. Bode Diagram of the closed-loop control strategy. (a) Tracking performance. (b) Antidisturbance performance.

the ESO parameters and keeps a good performance in a wide frequency range, which means that the control scheme keeps stable and robust in a wide range. And the diagram proves that the low-frequency disturbance, both the internal and external disturbance, has been successfully eliminated in the proposed control strategy.

D. Performance Comparison With Other Strategies

In order to investigate the proposed current harmonic suppression strategy based on ESO further, performance comparison with other strategies, in theory, is carried out. Using the PI controller in the z_1-z_2 current loop is the most common method at present, as shown in Fig. 2. It is easy to implement, stable, and effective. As for the advanced PR controller, unlike the PI controller, it is a model-based controller aiming for suppressing harmonics with certain order(s) without causing resonance to the system. So they are chosen to compare with the proposed ESO strategy. The bode diagrams on tracking performance and antidisturbance ability of the traditional PI controller and the advanced PR controller are given to compare with the proposed ESO strategy.

The closed-loop control law of the PI controller can be shown in (23), and it can be rearranged as (24)

$$\begin{cases} sx_1 = f + \frac{u_z}{L_{aa1}} \\ e = y^* - x_1 \\ u = \frac{k_i + k_p s}{s} e \end{cases} \tag{23}$$

$$\frac{L_{aa1}s^2 + k_p s + k_i}{s} x_1 = L_{aa1} f + \frac{k_i + k_p s}{s} y^*. \tag{24}$$

Similar to (21) and (22), the closed-loop transfer function and the sensitive transfer function from total disturbance to the system output of PI controller are derived as (25) and (26), respectively

$$G_{1\_PI} = \frac{y}{y^*} = \frac{\frac{k_i}{L_{aa1}} + \frac{k_p}{L_{aa1}} s}{s^2 + \frac{k_p}{L_{aa1}} s + \frac{k_i}{L_{aa1}}} \tag{25}$$

$$G_{2\_PI} = \frac{y}{f} = \frac{s}{s^2 + \frac{k_p}{L_{aa1}} s + \frac{k_i}{L_{aa1}}}. \tag{26}$$

The classical PR controller is not robust and easy to induce resonance. So the advanced PR controller is proposed either by fixing the phase interruption [32] or by inducing a bandwidth to widen the resonant frequency into a range and lower the resonant gain [33]. The latter strategy is utilized here since it is easier to achieve and has less calculation burden. The closed-loop control law of the advanced PR controller can be shown as

$$\begin{cases} sx_1 = f + \frac{u_z}{L_{aa1}} \\ e = y^* - x_1 \\ u = (k_p + \frac{k_i \omega_c s}{s^2 + 2\omega_c s + (5\omega_e)^2} + \frac{k_i \omega_c s}{s^2 + 2\omega_c s + (5\omega_e)^2}) e. \end{cases} \tag{27}$$

The closed-loop transfer function and the sensitive transfer function from total disturbance to the system output of the advanced PR controller are derived as follows:

$$G_{1\_\mathrm{PR}} = \frac{y}{y^*} = \frac{k_p + \frac{k_i \omega_c s}{s^2 + 2\omega_c s + (5\omega_e)^2} + \frac{k_i \omega_c s}{s^2 + 2\omega_c s + (7\omega_e)^2}}{L_{aa1} s + k_p + \frac{k_i \omega_c s}{s^2 + 2\omega_c s + (5\omega_e)^2} + \frac{k_i \omega_c s}{s^2 + 2\omega_c s + (7\omega_e)^2}} \tag{28}$$

$$G_{2\_\mathrm{PR}} = \frac{y}{f} = \frac{L_{aa1}}{L_{aa1} s + k_p + \frac{k_i \omega_c s}{s^2 + 2\omega_c s + (5\omega_e)^2} + \frac{k_i \omega_c s}{s^2 + 2\omega_c s + (7\omega_e)^2}}. \tag{29}$$

G_{1_PI} and $G_{1\cdot PR}$ reflect the tracking performance of the closed-loop controller. $G_{2\cdot PI}$ and $G_{2\cdot PR}$ reflect the antidisturbance ability of the related strategy. Their bode diagrams can be drawn in Fig. 9. The controller parameters are optimally tuned. The value of k_p and k_i remain the same in all three strategies. The bandwidth ω_0 of the ESO is chosen as 5000 rad/s, and the fundamental frequency of the current is chosen as 30 Hz.

Some conclusions can be concluded from Fig. 9.

a) The outputs of all three control strategies can successfully trace the magnitude of the speed reference until the frequency reaches about 1600 Hz. The PR controller has the worst tracking performance. A phase delay occurs when the frequency is over 160 Hz, which will lead to a time delay in tracking the speed reference. Also a fluctuation in both the magnitude and the phase occurs at about 48 Hz, which might cause a severe distortion when the frequency component locates nearby.

b) The tracking performance of ESO is the best. It would not induce phase delay or magnitude difference until over 160 000 Hz, which is far beyond the motor system, compared to 1600 Hz in PI controller.

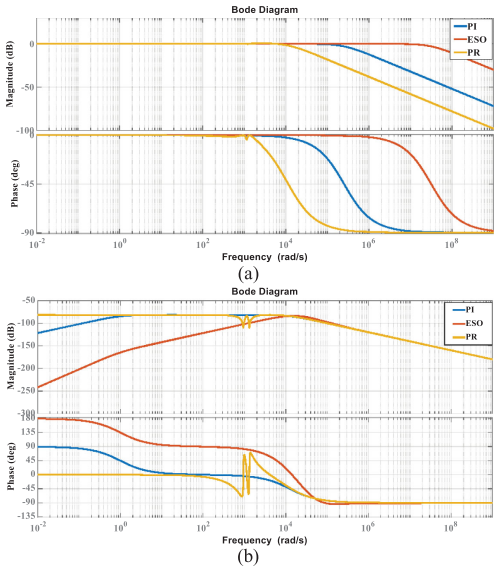

Fig. 9. Control performance comparison of PI, PR, and ESO. (a) Tracking performance. (b) Disturbance suppression performance.

c) All three control strategies have the ability to disturbance suppression as they are all close-loop controllers. The comparison can be divided into three parts: low-frequency region, middle-frequency region, and high-frequency region. When the fundamental frequency is under 16 Hz, the disturbance rejection ability of the ESO is far better than the other two strategies. In middle-frequency range, between 16 and 1600 Hz, where the important frequency components mainly located, the PI controller has the worst disturbance suppression ability. The advanced PR controller has almost the same effect as the PI controller except two suppression peaks at the 5th and 7th frequency components. The advanced PR controller can suppress the target frequency over 1/100. The disturbance rejection effect of ESO in this frequency range is better than PI in the whole range. The suppression effect of the ESO is better as the frequency decrease.

From the analysis above, compared with the PI controller and the advanced PR controller, the system with ESO has a better tracking performance and disturbance rejection ability in the whole working frequency without causing system degradation, which proves the advantages of ESO in theory.

IV. Applicability and Limitations of the Proposed Strategy

A lot of factors and different working conditions in the DTP-PMSM system will affect the current harmonics. This section will discuss the effectiveness and limitations of the proposed strategy under several conditions.

A. Magnetic Circuit Saturation

In Section II, it is assumed that the magnetic circuit is linear and magnetic saturation is ignored. In practical, most of the automotive drives need to have overload capabilities, in which the magnetic circuit is not linear anymore. The saturation in the material will affect the magnetic flux, inductance, leakage inductance, and then the output torque and current harmonics of the motor.

TABLE I
Parameters of the DTP-PMSM

Parameter	Symbol	Value
DC bus voltage	U_{DC}	$105V$
Switching frequency	f	$10kHz$
d-axis inductance	L_d	$8\times10^{-3}H$
q-axis inductance	L_q	$8\times10^{-3}H$
Leakage inductance	L_{aal}	$8\times10^{-4}H$
Stator resistance	R_s	0.8Ω
Flux linkage of magnet	Ψ_f	$0.35W_b$
Inertia	J	$0.045kg\cdot m^2$
Pole pairs	P_n	10
Rated speed	n	160rpm
Rated torque	T	7Nm
Rated current	I_{phase}	1.6A

Since the voltage equation and flux equation remain the same under magnetic saturation, the ESO strategy when saturation can still be presented as (12). The only difference is that the value of the leakage inductance (L_{aa1}) might change when saturated [37]. While the change of L_{aa1} might not have an obvious effect since the ESO is not sensitive to parameter change as shown in [20].

To prove the previous inference, finite-element analysis is applied to see the change of the inductance when saturated based on the parameters in Table I. The phase current is given as twice as the rated phase current at the rated speed and the inductance can be calculated. The results show that saturation would also change L_{aa1}, but it will only decrease slightly, less than 10%.

Furthermore, the close-loop ability of the proposed strategy can be shown in (21) and (22). Assuming that the leakage inductance varies by an order of magnitude, from 0.2 to 1 mH, if other parameters remain the same under magnetic saturation, the tracking performance (G1) and the antidisturbance ability (G2) can be shown in Fig. 10, where the bandwidth is chosen as 5000. The tracking performance and the antidisturbance ability of the proposed strategy remain effective when the leakage inductance changes without tuning any parameters. Besides, under overload conditions, the phase current will basically not reach twice the rated current, so the leakage inductance will not change much. It means that the proposed ESO strategy is adaptive in nonlinear magnetic circuits (saturation) without tuning any parameters.

In addition, Fig. 10 shows that the proposed strategy with different values of leakage inductance will still have a good tracking performance and antidisturbance performance. It will keep effective even though the leakage inductance is not measured or calculated accurately. The performance of ESO is not sensitive to leakage inductance or other parameters, which is consistent with previous research results [20].

B. Anisotropic Machines

The prototype and former analysis are based on the isotropic machines, as shown in Table I. As for the anisotropic machines,

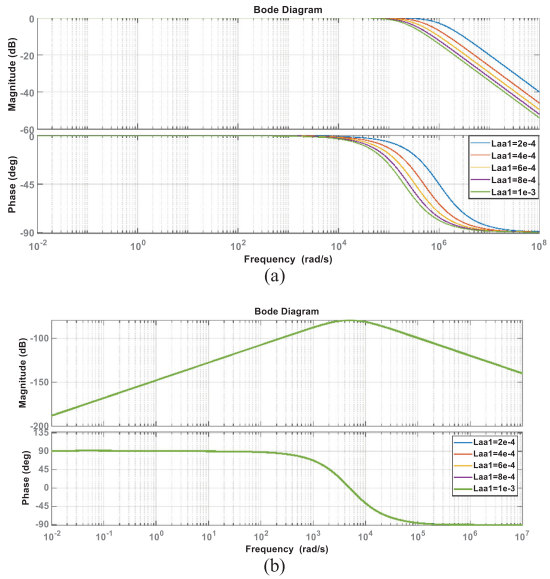

Fig. 10. Control performance comparison with different L_{aa1}. (a) Tracking performance. (b) Antidisturbance performance.

if the voltage equation in z_1-z_2 subspace is the same as the one in isotropic machines, the ESO strategy will still be effective in anisotropic machines. If not, the control scheme may need modification or ineffective in anisotropic machines.

Assume L_0 is the main self-inductance and L_2 is the second harmonic amplitude of the main self-inductance. In isotropic machines, L_2 equal to 0 while L_2 is not 0 in anisotropic machines. The inductance matrix in anisotropic machines in *d*-*q* axis is deduced as Eqn. (30) shown at the bottom of this page.

Substituting the inductance matrix of the anisotropic machines above into the voltage equation shown in (7) and (8), the voltage equation of the anisotropic machines in z_1-z_2 subspace is the same as the one in isotropic machines.

The anisotropy will only bring change to *d*-*q* subspace but will not affect z_1-z_2 subspace or o_1-o_2 subspace. Since the proposed ESO strategy works on z_1-z_2 subspace, it is still effective both in isotropic machines and in anisotropic machines without any modifications or parameter changes.

C. Nonideality of Inverters, Overmodulation, and SVPWM Strategies

Nonlinear characteristics of the inverter will cause voltage distortion and it is mainly induced by the dead time, on-state voltage drop of switching device, and freewheeling voltage drop of diode [35], [36]. According to [36], the error voltage can be equivalent to a square-wave signal so a large number of odd harmonic components are introduced into the DTP-PMSM system due to the existence of the dead zone effect and the voltage drop of the switching devices, mainly 5th and 7th voltage harmonics, $u_{5\text{th}\cdot\text{err}}$ and $u_{7\text{th}\cdot\text{err}}$. According to (5), the error voltage caused by the voltage drop and dead zone will only occur in $z1$-$z2$ subspace, shown as

$$T_{62s}u_{5th\_err} = \frac{1}{3}\begin{bmatrix} 1 & -\frac{1}{2} & -\frac{1}{2} & \frac{\sqrt{3}}{2} & -\frac{\sqrt{3}}{2} & 0 \\ 0 & \frac{\sqrt{3}}{2} & -\frac{\sqrt{3}}{2} & \frac{1}{2} & \frac{1}{2} & -1 \\ 1 & -\frac{1}{2} & -\frac{1}{2} & -\frac{\sqrt{3}}{2} & \frac{\sqrt{3}}{2} & 0 \\ 0 & -\frac{\sqrt{3}}{2} & \frac{\sqrt{3}}{2} & \frac{1}{2} & \frac{1}{2} & -1 \\ 1 & 1 & 1 & 0 & 0 & 0 \\ 0 & 0 & 0 & 1 & 1 & 1 \end{bmatrix}$$

$$* \begin{bmatrix} u_{5\text{th\_err}}\cos 5\omega t \\ u_{5\text{th\_err}}\cos 5(\omega t - \frac{2\pi}{3}) \\ u_{5\text{th\_err}}\cos 5(\omega t + \frac{2\pi}{3}) \\ u_{5\text{th\_err}}\cos 5(\omega t - \frac{\pi}{6}) \\ u_{5\text{th\_err}}\cos 5(\omega t - \frac{5\pi}{6}) \\ u_{5\text{th\_err}}\cos 5(\omega t + \frac{\pi}{2}) \end{bmatrix} = \begin{bmatrix} 0 \\ 0 \\ u_{5\text{th\_err}}\cos 5\omega t \\ u_{5\text{th\_err}}\sin 5\omega t \\ 0 \\ 0 \end{bmatrix}$$

$$T_{62s}u_{7th\_err} = \frac{1}{3}\begin{bmatrix} 1 & -\frac{1}{2} & -\frac{1}{2} & \frac{\sqrt{3}}{2} & -\frac{\sqrt{3}}{2} & 0 \\ 0 & \frac{\sqrt{3}}{2} & -\frac{\sqrt{3}}{2} & \frac{1}{2} & \frac{1}{2} & -1 \\ 1 & -\frac{1}{2} & -\frac{1}{2} & -\frac{\sqrt{3}}{2} & \frac{\sqrt{3}}{2} & 0 \\ 0 & -\frac{\sqrt{3}}{2} & \frac{\sqrt{3}}{2} & \frac{1}{2} & \frac{1}{2} & -1 \\ 1 & 1 & 1 & 0 & 0 & 0 \\ 0 & 0 & 0 & 1 & 1 & 1 \end{bmatrix}$$

$$* \begin{bmatrix} u_{7\text{th\_err}}\cos 7\omega t \\ u_{7\text{th\_err}}\cos 7(\omega t - \frac{2\pi}{3}) \\ u_{7\text{th\_err}}\cos 7(\omega t + \frac{2\pi}{3}) \\ u_{7\text{th\_err}}\cos 7(\omega t - \frac{\pi}{6}) \\ u_{7\text{th\_err}}\cos 7(\omega t - \frac{5\pi}{6}) \\ u_{7\text{th\_err}}\cos 7(\omega t + \frac{\pi}{2}) \end{bmatrix} = \begin{bmatrix} 0 \\ 0 \\ u_{7\text{th\_err}}\cos 7\omega t \\ -u_{7\text{th\_err}}\sin 7\omega t \\ 0 \\ 0 \end{bmatrix}. \quad (31)$$

Since $z1$-$z2$ subspace is not related to energy conversion, $u_{5\text{th}\cdot\text{err}}$ and $u_{7\text{th}\cdot\text{err}}$ will not cause torque ripple in the DTP-PMSM system but will cause a larger 5th and 7th harmonic current. The harmonic current components caused by the nonlinear characteristics of the inverter will be suppressed by the proposed ESO strategy.

In practice, the voltage drop in switching devices varies with operating conditions such as motor frequency and the dead time varies with many factors such as device characteristics. While according to Figs. 6(b), (d), and 8(b), the disturbance tracking ability and disturbance suppression ability are not affected by the value of the disturbance. So the effectiveness of the ESO strategy will not be affected by the uncertainty of the voltage drop and dead time.

$$L_{dq} = \begin{bmatrix} L_d = L_{aa1} + 3L_0 + 3L_2 & 0 & 0 & 0 & 0 & 0 \\ 0 & L_q = L_{aa1} + 3L_0 - 3L_2 & 0 & 0 & 0 & 0 \\ 0 & 0 & L_{aa1} & 0 & 0 & 0 \\ 0 & 0 & 0 & L_{aa1} & 0 & 0 \\ 0 & 0 & 0 & 0 & L_{aa1} & 0 \\ 0 & 0 & 0 & 0 & 0 & L_{aa1} \end{bmatrix} \quad (30)$$

The current harmonics will also be affected by the modulation ratio [37], especially in the overmodulation region. When operating in the overmodulation region, sometimes the duty cycle is full. When the PWM duty cycle is full, the ESO cannot perform well in harmonic suppression since the feedforward part is in front of the modulation part. But ESO still shows better ability in the overmodulation region since the overmodulation still induces $6k\pm1 (k = 1,2,3,\ldots)$ harmonic current components as shown in [37].

As for the three SVPWM strategies introduced in Section II, since two vector SVPWM ignores the $z1$-$z2$ subspace, the ESO strategy could not be utilized to suppress the current harmonics in two vector SVPWM. But the strategy can be utilized in four-vector SVPWM and three-phase decomposition SVPWM.

D. Speed of the System

According to (19), the choice of the bandwidth of ESO, ω_0, is mainly restricted by two aspects: 1) the fundamental frequency of phase current, and the step size of the algorithm. The frequency is decided by the speed and pole pairs of the DTP-PMSM, and the step size of the algorithm is restricted by the microprocessor. If the fundamental frequency of phase current is relatively large and the frequency of the CPU is relatively low, the proposed strategy might not have an effective ω_0. When the step size is 1/10 KHz, the basic frequency should be less than 769 Hz; if $2p = 8$, the speed should be less than 11 535 r/min. And if the step size is smaller, the speed range would rise. It means that the proposed strategy could be utilized in most of the applications considering the speed range.

V. Simulation and Experiment Results

A. Experimental Setup

In order to validate the effectiveness of the proposed strategy, simulation and experiments are carried out. The main DTP-PMSM parameters are presented in Table I. The prototype is designed with more poles, a low-speed range, and the relatively low slot filling factor. Since a more severe harmonic distortion exists under low frequency, the prototype with a lower operating frequency is more suitable to verify the advantages of the proposed strategy at low-frequency range, which is proved in theory in Section III-D. The experiment platform is set up, whose diagram and photograph are shown in Figs. 11 and 12.

The platform consists of a six-phase PMSM, which is controlled by one set of control board based on TMS320F28335DSP and two sets of the driving board based on IGBT. The sampling frequency of the current loop is 10 kHz. And the frequency of the speed loop is 1 kHz. The current feedback is measured by current sensors, disposed by conditioning circuit and transferred to DSP. The position signals are collected by a rotating transformer.

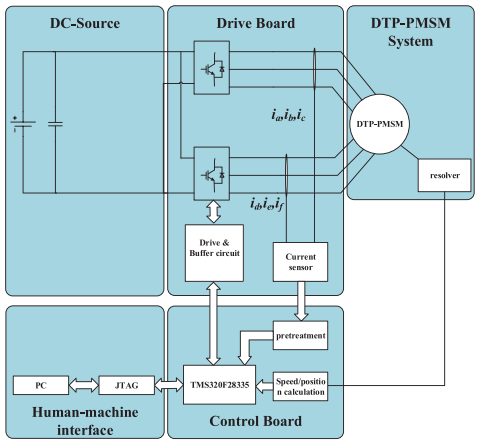

Fig. 11. Scheme of the experiment setup.

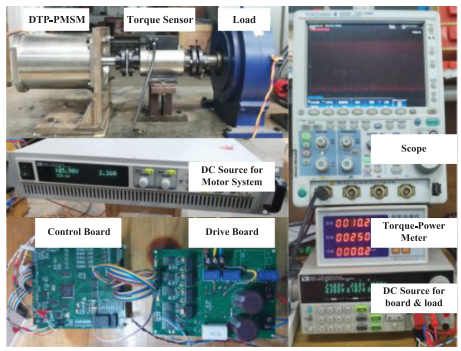

Fig. 12. Experiment platform.

B. Performance Analysis of the Strategy Based on the ESO

1) Simulation: First, the performance of the DTP-PMSM, when the current loop in the *d-q* subspace uses the PI controller and the current loop in $z_1 - z_2$ subspace uses the PI, PR, and ESO controller, is compared. The simulation model for PI is built based on Fig. 2, and the model for ESO is built based on Fig. 5.

The simulation not only studies the total harmonic distortion (THD) and the 5th, 7th harmonic current components under different control strategies but also compares the effect to the harmonic current distortion under different PWM modulation strategies, the nonideality of inverters and dead time.

According to Section IV-C, only the comparison between the four-vector SVPWM strategy and the three-phase decomposition SVPWM strategy is carried out.

The nonideality of inverters is also a potential influential factor of the harmonic current. In the simulation, the ideal inverters, which provide only the switching function without considering the properties of the electronic components, dead time, and real inverter, as shown in Section IV-C, are taken into the simulation separately.

The simulation results can be shown in Fig. 13. The *ideal_2sv* in Fig. 13 means that the modulation strategy is three-phase decomposition SVPWM strategy and the inverter model is ideal. And, *real_4sv* in Fig. 13 means that the modulation strategy is four-vector SVPWM strategy and the inverter model is real. Similarly, the meaning of *ideal_4sv* and *real_2sv* can be clear. To provide fair comparisons, the proportional coefficients (P) and integral coefficients (I) in the proposed ESO strategy and

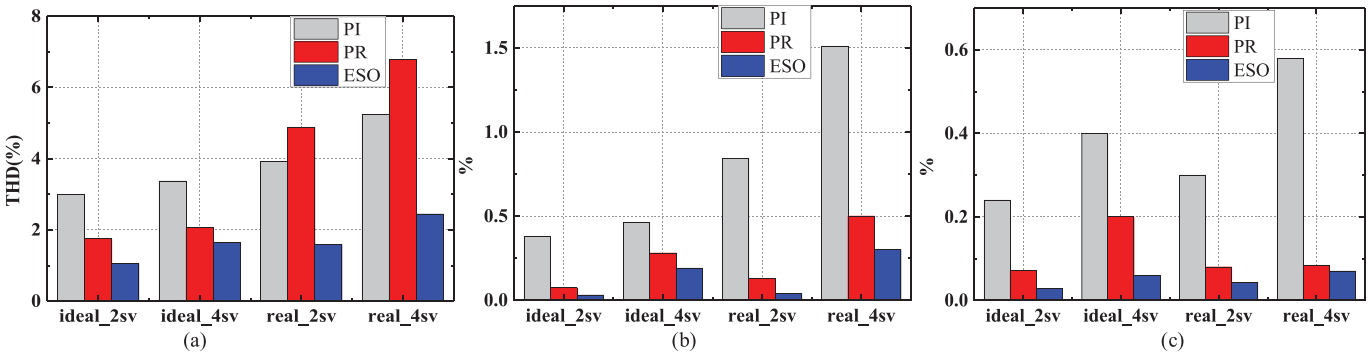

Fig. 13. Simulation results of THD under PI, PR, ESO controller, different PWM strategy, and different inverter models. (a) THD. (b) 5th harmonic. (c) 7th harmonic.

PR strategy are the same as the parameters in all PI controllers of conventional PI strategy.

Some conclusions can be summarized as follows.

(a) Compared to the conventional PI controller in the harmonic current loop, both the PR controller and the ESO can reduce the THD when the inverter model is ideal. The harmonic current suppression effect of ESO will surpass that of PR. While in the real inverter model, the THD under the PR controller outweighs that of PI controller under some occasions, which is caused by the resonance induced by the PR controller. The ESO in the real inverter model still has a desirable performance in current harmonic suppression.

(b) As for the 5th and 7th harmonic current, which are the important components of the harmonic current, both PR and ESO can successfully suppress these two components regardless of the PWM modulation strategies and modeling methods. And the suppression effect of ESO is better than that of PR.

(c) As for the PWM modulation strategies, the harmonic current content of three-phase decomposition SVPWM will be less than that of four-vector SVPWM, either the THD or the 5th, 7th harmonic current.

(d) The real modeling strategies of inverter increase not only the THD but also the percentage of 5th and 7th harmonic current, which proves that the nonlinearities of the practical inverter are also a main source of the 5th and 7th harmonic current. And the harmonic current components caused by the nonlinear characteristics of the inverter will be suppressed by the proposed ESO strategy. It matches the conclusion deduced in Section IV-C.

Another difference between the PR and ESO is that the PR controller only suppresses certain orders of the harmonic current, in this case, indicting the 5th and 7th harmonic current, whereas ESO suppresses all the harmonic components due to its theoretical characteristics, which is another advantage of ESO.

2) Experiments: According to the simulation results, the three-phase decomposition SVPWM is chosen as the PWM modulation strategy in an experiment for its advantage in harmonic reduction. To provide fair comparisons, the proportional coefficients (P) and integral coefficients (I) in the proposed ESO strategy and PR strategy are still the same with the parameters in the conventional PI strategy.

The experimental results of the proposed ESO control strategy are given, along with the results of the PI control strategy and advanced PR strategy. The waveforms of the phase A current under different control strategies are shown in Fig. 14, with the load of 11 N·m and the speed of 100 r/min. And their FFT analyses are given in Fig. 15 to verify the harmonic components.

The motor speed is 100 r/min, so the frequency of the fundamental wave is 16.67 Hz. According to Fig. 14, the waveforms of the phase current show that the proposed harmonic suppression strategy can successfully improve the sinusoid of the waveform compared to the PI controller, with obvious distortion at the zero-crossing point and peak, and advanced PR controller, with spikes at the top of the waveform. According to Fig. 15, the 5th and 7th harmonic current with PI controller are about 0.4 A, while they became about 5 mA with PR controller and ESO. So both ESO and PR controller can suppress the 5th and 7th harmonic current in the experiment. But in the PR controller, a current peak, which does not exist in the PI controller, is located at about 20 Hz. Besides, as the speed changes, the frequency of this current peak changes. It shows that although mitigated, slight resonance still exists in the PR controller. Besides, the value of the fundamental wave changes from 1.6 A when using PI to about 1.8 A when using ESO, promoting efficiency. So the ESO strategy is more effective in DTP-PMSM harmonic current suppression at this working condition.

Since the strategies aim to control the current in z_1-z_2 subspace, comparisons of the current in z_1-z_2 subspace will be more intuitive and convincing. The waveforms of the current in z_1-z_2 subspace with the PI controller and the proposed controller are shown in Fig. 16. Fig. 16(a) and (c) shows that the mainstream harmonic components in $z1$-$z2$ subspace is 5th and 7th harmonic components. Fig. 16(a) and (b) proves that the proposed ESO strategy successfully suppresses the harmonic currents in the $z_1 - z_2$ subspace.

In order to test the effectiveness of the strategy further, the phase current and its FFT analysis are measured at different speed and load. The waveform of the phase A current based on

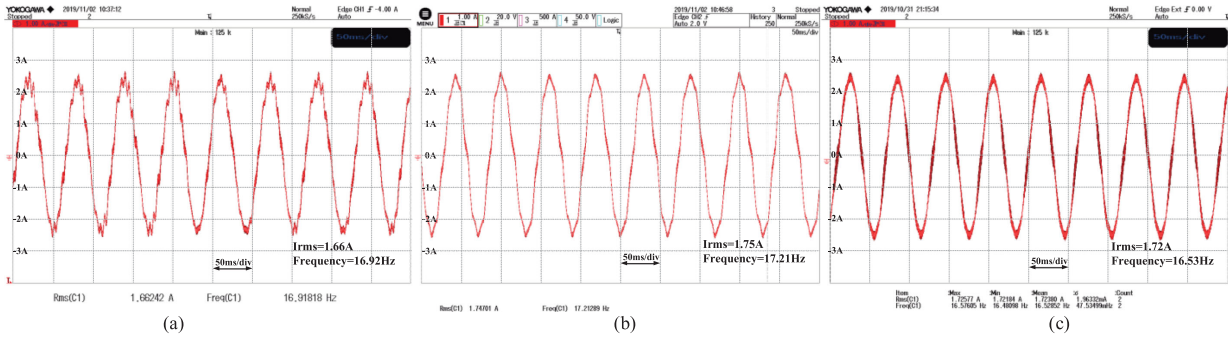

Fig. 14. Waveforms of the phase A current under different control strategies. (a) Waveform of the PI controller. (b) Waveform of PR controller. (c) Waveform of ESO controller.

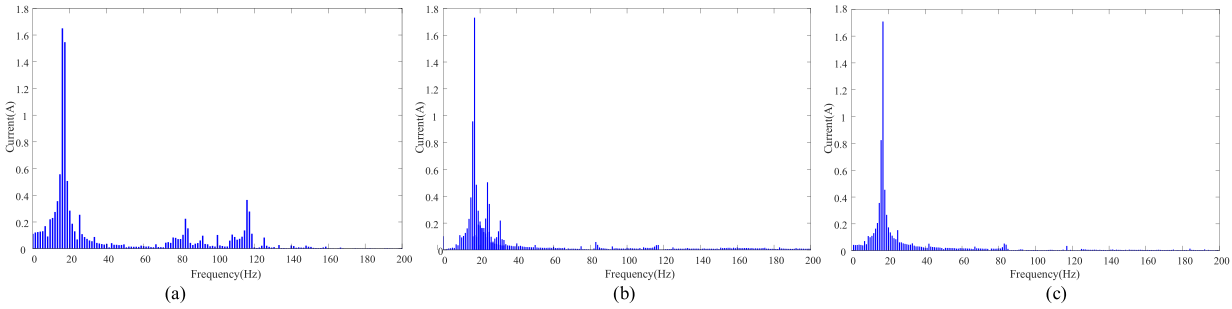

Fig. 15. FFT of phase current with different control strategies. (a) PI controller. (b) PR controller. (c) Extended state observer.

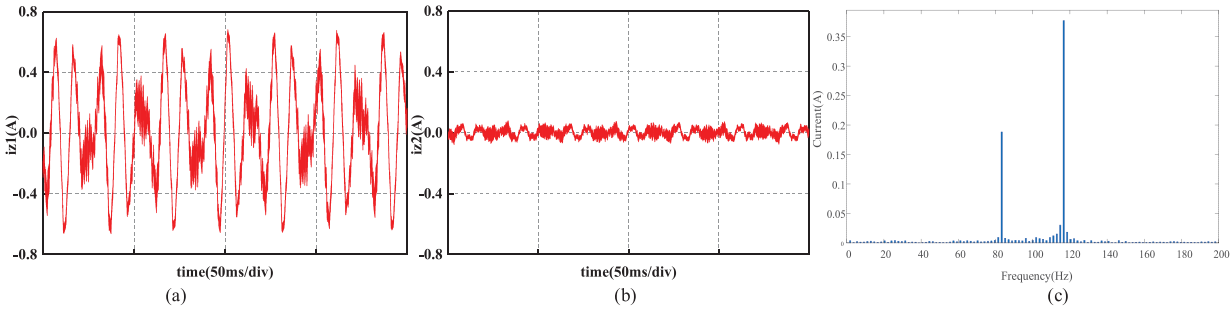

Fig. 16. Current waveform in $z1$-$z2$ subspace in different control schemes. (a) PI controller. (b) ESO controller. (c) FFT analysis in the PI controller.

the ESO with the same load (11 N·m) and different speed can be shown in Fig. 17.

The strategy based on ESO, advanced PR and PI controller are all tested at the speed of 60, 100, 150, 200, and 250 r/min with a load of 0, 2, 4, 7, and 11 N·m, respectively, to verify the effectiveness of the proposed strategy. The control strategy based on ESO can keep effective in all circumstances.

The THD of the phase current with these three strategies under different speed and load are calculated and compared. The results show that the THD almost keeps constant when the speed changes in all three strategies and changes when the load changes. The relationship between the load and THD with three strategies at the speed of 200 r/min can be represented in Fig. 18 and the THD calculation range cuts to 25th current harmonic.

It can be concluded from Fig. 18 that the PI controller at different load has a high level of THD. The advanced PR controller reduces the THD when the motor operates with the load. By comparison, the THD of the controller with ESO is the lowest in the whole load range, fluctuating at 3%. So the ESO can successfully suppress the current THD with different speed and load.

The THD changes with load under all three control strategies, higher when operating with no load or a light load. When operating at no load or light load, the uncertainty of the dry friction on the motor shaft makes the harmonic components more complex and a higher THD.

The advanced PR controller might operate worse under this condition since the components are more complex and more likely to encounter resonance. When the load increases, the THD decreased from 10% to about 6%.

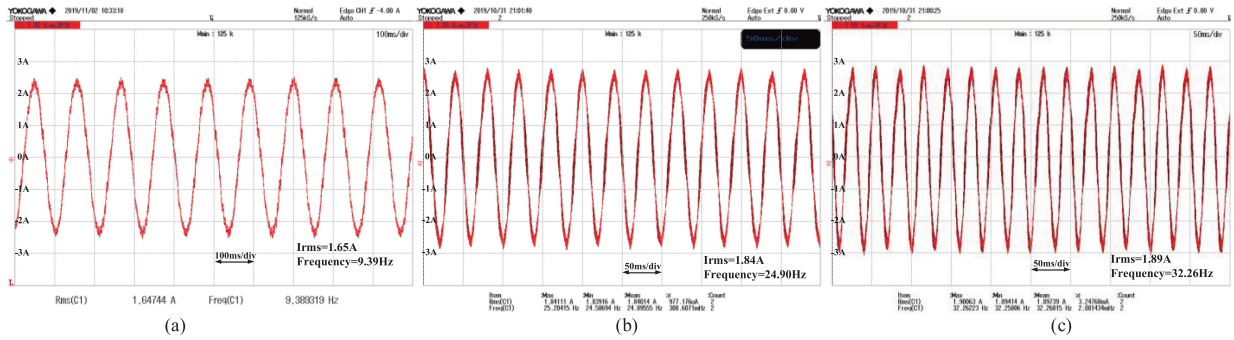

Fig. 17. Current waveform with ESO under different speed (a) 60 r/min, (b) 150 r/min, and (c) 200 r/min.

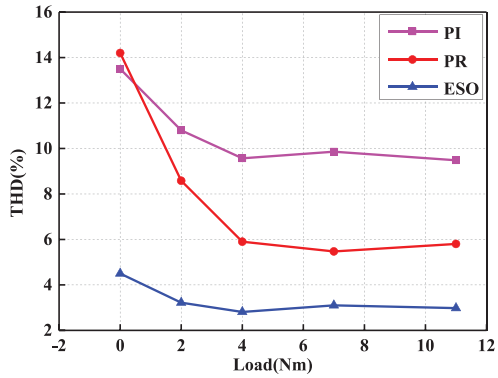

Fig. 18. Current THD comparison of PI, PR, and ESO at 200 r/min with different loads.

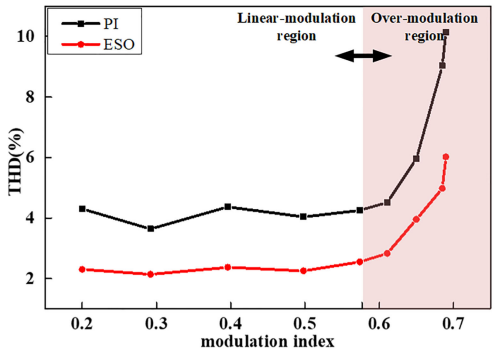

Fig. 20. Current THD comparison of PI and ESO with different modulation ratios.

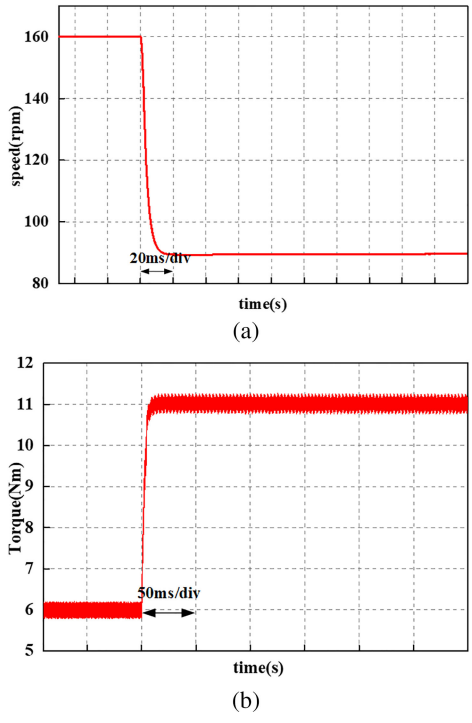

Fig. 19. Dynamic response of the proposed ESO strategy. (a) Speed response. (b) Torque response.

The complicated harmonic condition can also be regarded as a disturbance and can be observed by ESO. According to Fig. 18, the THD when utilizing ESO decreased from 14% to 4%. And, when the load increases, the THD with ESO is lower than the advanced PR controller since the ESO works on the whole frequency range, whereas the PR controller only focuses on 5th and 7th current harmonic components.

To verify the good dynamic characters of the ESO, the transient response of the speed changing from 160 to 90 r/min and the torque changing from 6 to 11 N·m in the ESO strategy is shown in Fig. 19.

The results in Fig. 19 show that the novel control strategy has good torque-tracking performance and speed-tracking performance. It proves that the transient response of the novel strategy is relatively quick and accurate.

In order to test the harmonic suppression ability with different modulation ratios, the figure of the THD in the PI controller and the ESO strategy with different modulation ratio are shown in Fig. 20. The working condition is chosen as 160 r/min and 11 N·m. The modulation index is changed by tuning the dc voltage. The range of U_{dc} changes from 180 to 55 V. And the modulation index changes from 0.2 to 0.7, respectively.

As the modulation index rises, when operating in the linear modulation range, the THD fluctuates either in the PI controller or in the ESO controller, and the trend is the same in both

schemes. And in the overmodulation region, the THD arises in both schemes.

In contrast, the strategy with ESO still shows better ability in overmodulation region compared to the PI controller. It matches the conclusion deduced in Section IV-C. In overmodulation region, although the suppression effect will decrease as the modulation index increase, the strategy with ESO is still effective.

Besides, for the conventional technique, the minimum dc bus voltage is 53 V. For the proposed technique, the minimum dc bus voltage is 50 V. Since the ESO strategy includes a feedforward part for $uz1$ and $uz2$, the voltage in $z1$-$z2$ subspace is more likely to be zero. That is another advantage of the novel strategy.

The possible limitations can be summarized as follows. It cannot be utilized in two vector SVPWM modulation strategy since it ignores the $z1$-$z2$ subspace. In the overmodulation range, as the modulation index rises, the ability of harmonic suppression will be undermined. Besides, a more powerful microprocessor should be implemented to carry out the proposed algorithm if the ESO is utilized in relatively high-speed machines to provide a smaller step size.

So the proposed harmonic suppression strategy based on ESO is an effective strategy for the DTP-PMSM drive system and it provides a high-performance alternative to the conventional harmonic control in multiphase PMSMs.

VI. Conclusion

In this article, a novel current harmonic suppression method for DTP-PMSM is proposed to solve the current distortion problem inherent in such motors. The main idea of this strategy is to treat the sources of the current distortion as a total disturbance and eliminate it with the proposed ESO scheme. The effectiveness and advantages of the scheme are proved by theory. The discussion also shows that both the ESO and the closed-loop control system remain robustly stable against uncertainties under a wide frequency range.

The following merits of the proposed strategy based on ESO can be concluded in comparison with the ordinary four-dimensional vector control strategy based on the PI controller and a conventional harmonic suppression strategy, advanced PR controller.

1) Less parameters are needed to tune in the proposed strategy, only the bandwidth of the ESO, while three parameters are needed in an advanced PR controller. Besides, the implementation of ESO is easier compared to the advanced PR controller, simply adding an ESO to the traditional PI controller without changing its structure. It also shows advantages such as robust, fast dynamic response, and parameter insensitivity. The advantages are especially obvious in the low-frequency range, in which the harmonic distortion is the most severe.
2) The proposed strategy suppresses the harmonics in the entire frequency domain without additional design. Compared to the advanced PR controller, the strategy with ESO can suppress other harmonic orders besides the 5th and 7th. The value of the fundamental current increases and the least dc voltage decreased when using ESO, promoting efficiency.
3) The proposed strategy is effective in a wide speed range. And it is also effective when the DTP-PMSM operates in a slight saturation mode without changing any parameters. The strategy can be utilized in both isotropic machines and anisotropic machines. The effect of the voltage-drop brought by the dead time, on-state voltage-drop of the switching device, and freewheeling voltage drop of the diode can be suppressed by the novel strategy. In the oversaturation range, the new strategy can still have a harmonic suppression effect.

References

[1] E. Levi, F. Barrero, and M. J. Duran, "Multiphase machines and drives—Revisited," *IEEE Trans. Ind. Electron.*, vol. 63, no. 1, pp. 429–432, Jan. 2016.

[2] F. Barrero and M. J. Duran, "Recent advances in the design, modeling, and control of multiphase machines—Part I," *IEEE Trans. Ind. Electron.*, vol. 63, no. 1, pp. 449–458, Jan. 2016.

[3] E. Levi, "Advances in converter control and innovative exploitation of additional degrees of freedom for multiphase machines," *IEEE Trans. Ind. Electron.*, vol. 63, no. 1, pp. 433–448, Jan. 2016.

[4] Z. Wang, X. Wang, M. Cheng, and Y. Hu., "Comprehensive investigation on remedial operation of switch faults for dual three-phase PMSM drives fed by T-3L Inverters," *IEEE Trans. Ind. Electron.*, vol. 65, no. 6, pp. 4574–4587, Jun. 2018.

[5] Y. Miyama, M. Ishizuka, H. Kometani, and K. Akatsu, "Vibration reduction by applying carrier phase-shift PWM on dual three-phase winding permanent magnet synchronous motor," *IEEE Trans. Ind. Appl.*, vol. 54, no. 6, pp. 5998–6004, Nov./Dec. 2018.

[6] H. Almarhoon, Z. Q. Zhu, and P. L. Xu, "Improved rotor position estimation accuracy by rotating carrier signal injection utilizing zero-sequence carrier voltage for dual three-phase PMSM," *IEEE Trans. Ind. Electron.*, vol. 64, no. 6, pp. 4454–4462, Jun. 2017.

[7] W. Wang, J. Zhang, M. Cheng, and S. H. Li, "Fault-tolerant control of dual three-phase permanent-magnet synchronous machine drives under open-phase faults," *IEEE Trans. Power Electron.*, vol. 32, no. 3, pp. 2052–2063, Mar. 2017.

[8] T. C. Lin, Z. Q. Zhu, K. Liu, and J. M. Liu, "Improved sensorless control of switched-flux permanent-magnet synchronous machines based on different winding configurations," *IEEE Trans. Ind. Electron.*, vol. 63, no. 1, pp. 123–132, Jan. 2016.

[9] C. Zhou, G. Yang, and J. Su, "PWM strategy with minimum harmonic distortion for dual three-phase permanent-magnet synchronous motor drives operating in the overmodulation region," *IEEE Trans. Power Electron.*, vol. 31, no. 2, pp. 1367–1380, Feb. 2016.

[10] H. X. Lu, J. Li, R. H. Qu, D. L. Ye, and Y. Lu, "Fault-tolerant predictive control of six-phase PMSM drives based on pulse-width-modulation," *IEEE Trans. Power Electron.,* vol. 66, no. 7, pp. 4992–5003, 2019.

[11] F. Barrero *et al.*, "An enhanced predictive current control method for asymmetrical six-phase motor drives," *IEEE Trans. Ind. Electron.*, vol. 58, no. 8, pp. 3242–3252, Aug. 2011.

[12] Y. Hu, Z. Q. Zhu, and K. Liu, "Current control for dual three-phase permanent magnet synchronous motors accounting for current unbalance and harmonics," *IEEE J. Emerg. Sel. Topics Power Electron.*, vol. 2, no. 2, pp. 272–284, Jun. 2014.

[13] Y. Ren and Z. Q. Zhu, "Enhancement of steady-state performance in direct-torque-controlled dual three-phase permanent-magnet synchronous machine drives with modified switching table," *IEEE Trans. Ind. Electron.*, vol. 62, no. 6, pp. 3338–3350, Jun. 2015.

[14] J. Karttunen, S. Kallio, P. Peltoniemi, and P. Silventoinen, "Current harmonic compensation in dual three-phase PMSMs using a disturbance observer," *IEEE Trans. Ind. Electron.*, vol. 63, no. 1, pp. 583–594, Jan. 2016.

[15] Y. Luo and C. Liu, "A simplified model predictive control for a dual three-phase PMSM with reduced harmonic currents," *IEEE Trans. Ind. Electron.*, vol. 65, no. 11, pp. 9079–9089, Nov. 2018.

[16] J. Karttunen, S Kallio, P. Peltoniemi, P. Silventoinen, and O. Pyrhönen, "Decoupled vector control scheme for dual three-phase permanent magnet synchronous machines," *IEEE Trans. Ind. Electron.*, vol. 61, no. 5, pp. 2185–2196, May 2014.
[17] J. Han, "From PID to active disturbance rejection control," *IEEE Trans. Ind. Electron.*, vol. 56, no. 3, pp. 900–906, Mar. 2009.
[18] H. X. Liu and S. H. Li., "Speed control for PMSM servo system using predictive functional control and extended state observer," *IEEE Trans. Ind. Electron.*, vol. 59, no. 2, pp. 1171–1183, Feb. 2012.
[19] L. S. Wang, M. Y. Wang, B. Guo, Z. Wang, D. Wang, and Y. L. Li., "Analysis and design of a speed controller for electric load simulators," *IEEE Trans. Ind. Electron.*, vol. 63, no. 12, pp. 7413–7422, Dec. 2016.
[20] M. Yang, X. Y. Lang, J. Long, and D. G. Xu., "Flux immunity robust predictive current control with incremental model and extended state observer for PMSM drive," *IEEE Trans. Ind. Electron.*, vol. 32, no. 12, pp. 9267–9279, Dec. 2017.
[21] X. Zhang and J. Q. Yang, "A DC-link voltage fast control strategy for high-speed PMSM/G in flywheel energy storage system," *IEEE Trans. Ind. Appl.*, vol. 54, no. 2, pp. 1671–1679, Mar./Apr. 2018.
[22] E. Schrijver and J. Van Dijk, "Disturbance observers for rigid mechanical systems: equivalence, stability, and design," *J. Dyn. Syst. Meas. Control*, vol. 124, pp. 539–548, 2002.
[23] D. Benrabah, G. Xu, and Z. Q. Gao, "Active disturbance rejection control of LCL-filtered grid-connected inverter using padé approximation," *IEEE Trans. Ind. Appl.*, vol. 54, no. 6, pp. 6179–6189, Nov./Dec. 2018.
[24] Y. F. Zhao and T. A. Lipo, "Space vector PWM control of dual three-phase induction machine using vector space decomposition," *IEEE Trans. Ind. Appl.*, vol. 31, no. 5, pp. 1100–1109, Sep./Oct. 1995
[25] R. Bojoi, E. Levi, F. Farina, A. Tenconi, and F. Profumo, "Dual three-phase induction motor drive with digital current control in the stationary reference frame," *IEE Proc.—Electr. Power Appl.*, vol. 153, no. 1, pp. 129–139, Jan. 2006.
[26] M. J. Duran, S. Kouro, B. Wu, E. Levi, F. Barrero, and S. Alepuz, "Six phase PMSG wind energy conversion system based on medium-voltage multilevel converter, " in *Proc. 14th Eur. Conf. Power Electron. Appl.*, 2011, pp. 1–10.
[27] H. Che, E. Levi, M. Jones, H. Ping, and N. Abd Rahim, "Current control methods for an asymmetrical six-phase induction motor drive," *IEEE Trans. Power Electron.*, vol. 29, no. 1, pp. 407–417, Jan. 2014.
[28] D. Hadiouche, L. Baghli, and A. Rezzoug, "Space-vector PWM techniques for dual three-phase AC machine: Analysis, performance evaluation, and DSP implementation," *IEEE Trans. Ind. Appl.*, vol. 42, no. 4, pp. 1112–1122, Jul./Aug. 2006.
[29] K. Marouani, L. Baghli, D. Hadiouche, A. Kheloui, and A. Rezzoug, "A new PWM strategy based on a 24-sector vector space decomposition for a six-phase VSI-fed dual stator induction motor," *IEEE Trans. Ind. Electron.*, vol. 55, no. 5, pp. 1910–1920, May 2008.
[30] G. Grandi, G. Serra, and A. Tani, "Space vector modulation of a six-phase VSI based on three-phase decomposition," in *Proc. Int. Symp. Power Electron., Elect., Drives, Autom. Motion*, 2008, pp. 674–679.
[31] R. Bojoi, A. Tenconi, F. Profumo, G. Griva, and D. Martinello, "Complete analysis and comparative study of digital modulation techniques for dual three-phase ac motor drives," in *Proc. IEEE 33rd Annu. Power Electron. Spec. Conf.*, 2002, pp. 851–857.
[32] L. Wang, M. Wang, B. Guo, Z. Wang, D. Wang, and Y. Li, "A loading control strategy for electric load simulators based on proportional resonant control, " *IEEE Trans. Ind. Electron.*, vol. 65, no. 6, pp. 4608–4618, Jun. 2018.
[33] K. Seifi and M. Moallem, "An adaptive PR controller for synchronizing grid-connected inverters, " *IEEE Trans. Ind. Electron.*, vol. 66, no. 3, pp. 2034–2043, Mar. 2019.
[34] T. H. Jung, G. H. Gwon, C. H. Kim, J. Han, Y. S. Oh, C.-H. Noh, "Voltage regulation method for voltage drop compensation and unbalance reduction in bipolar low-voltage DC distribution system," *IEEE Trans. Power Del.*, vol. 33, no. 1, pp. 141–149, Feb. 2017.
[35] C. Zhu, Z. Y. Zeng, and R. X. Zhao, "Torque ripple elimination based on inverter voltage drop compensation for a three-phase four-switch inverter-fed PMSM drive under low speeds," *IET Power Electron.,* vol. 10, no. 12, pp. 1430–1437, Jun. 2017.
[36] Z. Y. Zhang, X. L. Ge, Z. S. Tian, X. Zhang, Q. Tang, and X. Feng, "A PWM for minimum current harmonic distortion in metro traction PMSM with saliency ratio and load angle constrains," *IEEE Trans. Power Electron.*, vol. 33, no. 5, pp. 4498–4511, May 2018.
[37] M. Jecmenica, B. Brkovic, E. Levi, and Z. Lazarevic, "Interplane cross-saturation in multiphase machines," *IET Electr. Power Appl.*, vol. 13, no. 11, pp. 1812–1822, Nov. 2019.

Yongxiang Xu (Member, IEEE) was born in Guangxi Province, China, in 1977. He received the M.S. and Ph.D. degrees in electrical engineering from the Harbin Institute of Technology, Harbin, China, in 2001 and 2005, respectively.

He is currently a Professor with the School of Electrical Engineering, Harbin Institute of Technology. His current research interests include permanent-magnet machine design and control.

Boyuan Zheng was born in Liaoning Province, China, in 1992. He received the B.S. and M.S. degrees in electrical engineering in 2015 and 2017, respectively, from the Harbin Institute of Technology, Harbin, China, where he is currently working toward the Ph.D. degree.

His current research interests include dual three-phase permanent-magnet machine control and optimization.

Guan Wang was born in Liaoning Province, China, in 1994. He received the B.S. and M.S. degrees in electrical engineering from the Harbin Institute of Technology, Harbin, China, in 2016 and 2018, respectively.

His research interests include dual three-phase permanent-magnet machine drives.

Hao Yan (Member, IEEE) received the B.S., M.S., and Ph.D. degrees in electrical engineering from the Harbin Institute of Technology, Harbin, China, in 2011, 2013, and 2018, respectively.

He subsequently joined the Power Electronics, Machines and Control Group, University of Nottingham, Ningbo, China, and worked on power electronics for electrical drives for two years. He is currently a Research Fellow with the Rolls-Royce, NTU Corporate Lab, Nanyang Technological University, Singapore. His current research interests include permanent-magnet machine drives and power converters in more electric aircraft.

Jibin Zou (Senior Member, IEEE) was born in Heilongjiang Province, China, on January 19, 1957. He received the M.S. and Ph.D. degrees in electrical engineering from the Harbin Institute of Technology, Harbin, China, in 1984 and 1988, respectively.

Since 1985, he has been engaged in the research in electrical machines. He was with the University of Liverpool, Liverpool, U.K., as a Visiting Research Fellow for one year. He is currently a Professor with the State Key Laboratory of Robotics and System, Harbin Institute of Technology. His current research interests include permanent-magnet machine design and control.

Prof. Zou is a Senior Member of the IEEE Magnetics Society, since 2000.